Quantitative imaging of concentration by planar laser-induced fluorescence

I. van Cruyningen, A. Lozano, and R. K. Hanson

Dept. of Mechanical Engineering, Stanford University, Stanford, CA, 94305 USA

Abstract. The planar laser-induced fluorescence (PLIF) technique is attractive for instantaneous and non-intrusive imaging of species concentration in gaseous flows. This paper provides a framework for determining the experimental resolution in PLIF experiments and gives error estimates for concentration measurements in turbulent jet mixing experiments using biacetyl as the molecular tracer. The procedures to correct for experimental artifacts in the PLIF images are outlined. Images of the instantaneous, average, rms, and dissipation of concentration in a turbulent jet are presented.

1 Introduction

Planar imaging techniques provide a non-intrusive means of instantaneously determining concentration at all points in a cut through the flow. The flow is illuminated with a laser sheet and images are formed from light scattered by molecules in the flow (Hanson 1987). Fluorescence techniques exhibit some of the largest scattering cross-sections and have been demonstrated in liquids (Liu et al. 1977, Dimotakis et al. 1983, Dahm and Dimotakis 1987, and Shlien 1988), reacting flows (Kychakoff et al. 1982 and Dyer and Crosley 1982), and non-reacting gaseous flows (Kychakoff et al. 1987). Early work in quantifying the error sources in these techniques was presented by Kychakoff et al. (1984), Cattolica and Vosen (1985), Hiller (1986), Winter et al. (1987), and Allen (1987). Paul et al. (1990) advanced this work and described the selection of the optimum camera for a given experiment. This paper outlines the means for experimentally determining resolution limits and gives detailed error correction procedures. The analysis is applied to a set of turbulent mixing measurements using biacetyl as a tracer molecule in a turbulent jet, and images of the instantaneous, average, root-mean-square, and dissipation of concentration are presented.

2 Experiment

The setup for the turbulent jet experiment is illustrated in Fig. 1. Laser light from a pulsed XeF excimer laser (Questek 2,220, $\lambda = 351$ nm, ~ 90 mJ per 20 ns pulse with stable resonator optics) was formed into a thin sheet approx. 50 cm high and 600 μm thick. This sheet was double-passed through the center of a nitrogen jet flowing downward at 8.5 m/s from a 1 cm diameter vertical nozzle ($Re = 8,500$). A mirror reflected the sheet back through the flow for a second pass. The atmospheric pressure jet was seeded with the molecular tracer biacetyl (2-3 Butanedione) to a saturation concentration of 40 torr partial pressure ($\sim$ five percent mole fraction). A uniform coflow of 10 cm/s across the 60 cm $\times$ 60 cm tunnel prevented recirculation of the biacetyl and provided an ambient background of pure nitrogen.

The laser light excited the biacetyl molecules which subsequently either fluoresced with a decay time of 50 ns, phosphoresced with a decay time of 1.1 ms, or were collisionally deexcited. The broadband emitted light was imaged onto a cooled CCD array (Photometrics Model 81-S camera with 384×576 pixel Thompson CSF TH 7882-CDA array). The signal from the array was digitized and stored on an IBM AT computer. Final corrections and processing were done on a Sun 3/160C and Pixar Image Computer.

3 Laser characterization

In order to freeze the motion of the flow, PLIF experiments use either pulsed lasers or shuttered cw laser sources. Hence, the following analysis will be done on a per laser pulse basis. The laser can be characterized by its spectral fluence as distributed over space, time, and frequency, $\varepsilon(y, z, t, v)$ [J/cm^2 s Hz], using the coordinate system shown in Fig. 1. The time variation is important when acquiring multiple images from one pulse or if peak powers in the laser pulse can cause saturation of the fluorescence species. The frequency variation is important when the laser linewidth is equal to or larger than the absorption spectrum of the species probed; or if the laser and absorption lines have only a partial overlap. In these cases only part of the laser energy is available for inducing fluorescence. If the PLIF experiment uses a collimated sheet with a narrow laser linewidth
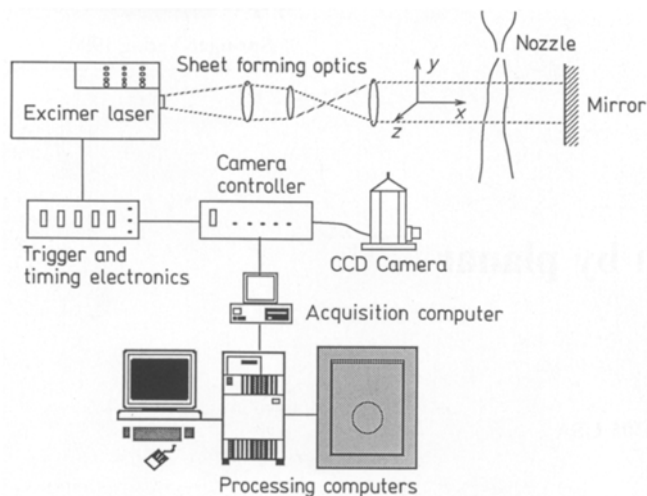
Fig. 1. Experimental apparatus

and one image is acquired per pulse, the variations in thickness, time, and frequency can all be integrated out. Only the variation with height remains important.

Optical beam irradiance for near monochromatic light can be specified either in terms of an energy flux or as the photon flux at the specified wavelength. To facilitate a shot noise determination, the remaining calculations in this paper shall be done in terms of number of photons. The laser can be characterized by the number of photons per unit height incident on the flow:

$$N_i'(y) = \frac{e(y)}{h\,v} = N_i\,\phi_i'(y) \tag{1}$$

where the prime on N_i denotes per unit height; $e(y)$ is the laser energy distribution per unit height in J/cm; $h = 6.63 \times 10^{-34}$ J s is Planck's constant; v is the laser centerline frequency in Hz; N_i is the total number of photons per pulse; and $\phi_i'(y)$ is the photon distribution in the y direction, normalized to integrate to 1.0.

For unstable resonator or high gain dye lasers the normalized photon distribution, $\phi_i'(y)$, may vary significantly from pulse to pulse. It must be measured using a linear array (or a second area array) for each image acquired. Stable resonator lasers with lower gain media, such as the XeF excimer used here, can provide more consistent energy distributions. Images of a static cell filled with biacetyl showed variations of less than 0.5% rms at any point in the sheet profile.

The rms fluctuation in the total number of photons per pulse, N_i (calculated by integrating the sheet profiles), was approx. 1.2%. The laser energy fluctuations are small, but they must be accounted for when 1) performing statistics on groups of images, 2) comparing images from a time series, or 3) constructing data volumes from three dimensional data sets. These variations can be compensated by either including a known concentration reference in each image, or by making an independent pulse energy measurement for each

image acquired. For jet flows, the potential core at the nozzle exit provides a known, fully seeded concentration as a point of reference. A Hamamatsu photodiode (S1723-05) was used as an independent energy measurement during acquisition of the turbulent jet images.

4 Species characterization

The species monitored in PLIF experiments is either seeded into the flow (e.g. biacetyl, O_2, I_2, NO, or fluorescein dye), or it is a radical produced as a result of a reaction (e.g. CH, OH, C_2, or CO). The laser light is tuned to excite a particular electronic transition in the tracer and a fraction of the molecules in the appropriate lower energy level absorb the incident light and transfer to the higher energy level. These excited molecules either emit a photon through spontaneous emission on short time scales (fluorescence); undergo transfer to a different electronic state and then emit light on a much longer time scale (phosphorescence); predissociate to lower electronic states; or collisionally quench with other molecules. The total light emission per unit sheet area for unsaturated excitation is given by:

$$N_e''(x, y, v, t)$$
$$= \{\text{Photons Incident per unit Height}\}$$
$$\cdot \{\text{Photons Absorbed per unit Length}\}$$
$$\cdot \{\text{Photons Emitted per Photon Absorbed}\}$$
$$= \{N_i'(y)\, e^{-(\alpha(v)+\sigma)\int C(x,y)\,dx}\}\, \{\alpha(v)\, C(x,y)\}\, \{\eta_s(v,t)\} \tag{2}$$

where the double prime on N_e'' denotes per unit area; $\alpha(v)$ is the absorption cross-section of the tracer in cm^2; σ is the Rayleigh scattering cross-section of the tracer in cm^2 (often negligible); $C(x, y)$ is the concentration of the absorbing species in cm^{-3} in the lower energy level; and $\eta_s(v, t)$ is the species 'quantum efficiency' or Stern-Vollmer factor for this transition.

The first term is the incident laser photon distribution derived in the previous section, attenuated by the absorption and scattering the beam has already encountered. The absorption coefficients for many species are available in the extensive spectroscopy literature. The optical depth is given by

$$l = \frac{1}{(\alpha+\sigma)\, C_{avg}} \tag{3}$$

where C_{avg} is an estimate of the average absorbing species concentration along the beam path.

If the extent of the flowfield is much less than the optical depth ($x \ll l$), the absorption of the laser beam is negligible and the exponential term can be ignored. This significantly simplifies the equation and makes it linear in the absorbing species concentration.

$C(x, y)$ is the concentration in the molecular energy level which is being depleted by the laser pumping. For gases at room temperature this is almost always the ground state and

$C(x, y)$ equals the species concentration. For radicals in reacting flows, the laser may induce transitions from a higher energy level, or a significant fraction of the radical population may exist in other energy levels (Vincenti and Kruger 1982). In these cases the radical concentration must be multiplied by the appropriate Boltzmann factors to determine $C(x, y)$.

The Stern-Vollmer factor, $\eta_s(v, t)$, contains all the details of the photon conversion process. It is a function of frequency and time because the excited species can fluoresce and phosphoresce into several different frequencies with different timescales. For diatomic or simple triatomic molecules the Stern-Vollmer factor can be estimated from the Einstein spontaneous (A) and stimulated (B) emission coefficients. A two-level model was developed by Piepmeier (1972) and extended for biacetyl emission by Liu et al. (1988). If 1 denotes the lower level, 2 the upper level, Q the quenching rate, and I the laser intensity,

$$\eta_s = \frac{A_{21}}{Q_{21} + A_{21} + (B_{12} + B_{21})I} \tag{4}$$

Unfortunately the largest term in the denominator, Q_{21}, is seldom known and difficult to predict.

For species stable at room temperature, this factor, η_s, can be established by measuring the emission from a static cell for known species concentrations and pulse energies. It should be independent of biacetyl concentration unless self-quenching occurs. The variation of emission with biacetyl concentration was measured in an atmospheric pressure static cell filled with nitrogen. For excitation with 1.4×10^{16} photons/cm^2 at 351 nm the emission is a linear function of concentration with 6.8×10^9 ($\pm 3\%$) photons/cm^2 emitted per torr of biacetyl partial pressure. This agrees with the measurements of Liu et al. (1988) for 435 nm excitation. The Stern-Vollmer factor should also be independent of laser power except near saturation of the transition. In the same static cell experiment the biacetyl emission was measured to be a linear function of incident photon density for the laser energy levels used in the image acquisition. For a biacetyl partial pressure of 32 torr and excitation at 351 nm, 1.3×10^{-5} ($\pm 2\%$) photons/cm^2 were emitted per photon/cm^2 incident. Neither self-quenching nor saturation occurred for the species concentrations or laser energies used in the turbulent jet experiments.

A prism spectrograph was used to determine the biacetyl emission spectrum and photomultiplier measurements were used to determine the phosphorescent and fluorescent lifetimes (van Cruyningen, 1990). The prism spectrograph allowed simultaneous measurements of both the fluorescence and phosphorescence emission for wavelengths between 430 and 600 nm. The spectrograph dispersion was first calibrated with a mercury lamp and then the variation in the array quantum efficiency over the wavelength range was determined from a tungsten source. Finally a static cell filled with 5% mole fraction biacetyl in one atmosphere nitrogen was excited by the excimer laser at 351 nm and the emission
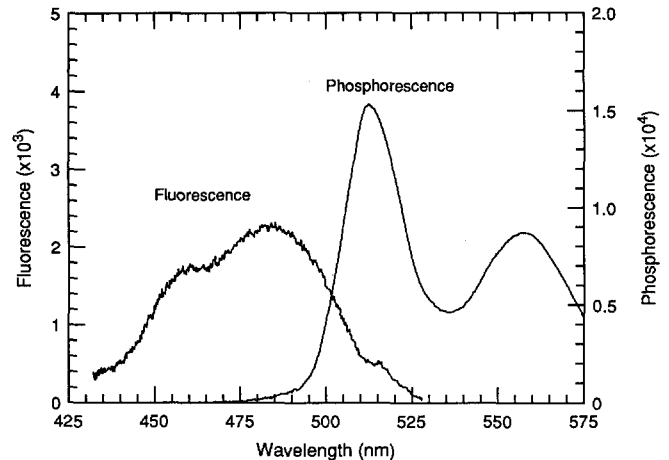

Fig. 2. Normalized biacetyl emission spectra for 351 nm excitation. Fluorescence and phosphorescence spectra normalized to unit area

imaged into the spectrograph. The rescaled emission spectra, $F_{fl}(v)$ and $F_{ph}(v)$, (Fig. 2) were normalized so that the integrals under each curve are equal. The ratio of phosphorescence to fluorescence emission integrated over time and wavelength, K_{ph}/K_{fl}, was measured to be 78 ($\pm 5\%$) in reasonable agreement with the measurements of Okabe and Noyes (1957). The measured Stern-Vollmer factor can be expressed as:

$$\eta_s(v, t) = K_{fl} F_{fl}(v) \exp(-t/\tau_{fl}) + K_{ph} F_{ph}(v) \exp(-t/\tau_{ph}) \tag{5}$$

where $F_{fl}(v)$ and $F_{ph}(v)$ are the normalized fluorescent and phosphorescent emission spectra (Fig. 2); K_{fl} and K_{ph} represent the strengths of the two types of emission; and $\tau_{fl} \cong 50$ ns and $\tau_{ph} \cong 1.1$ ms are the $1/e$ decay times for the fluorescent and phosphorescent emission respectively.

5 Collection optics characterization

The collection optics serve to image the fluorescence emission onto the camera. This usually includes one or more camera lenses, a filter to remove scattered laser light, and possibly an intensifier with fiberoptic coupler to provide signal gain. In addition to the signal level, the spatial resolution, geometric distortion, and flat field non-uniformity of the optics must be examined. This discussion summarizes procedures for experimentally determining the appropriate performance parameters; a more detailed discussion is given in Paul et al. (1990).

The number of photons per pixel reaching the camera is given by

$$N_{pp}(x, y, v, t) \tag{6}$$

$$= \{\text{Emission per unit Area}\} \{\text{Area}\} \left\{ \frac{\text{Solid Angle}}{4\pi} \right\}$$

$$\cdot \{\text{Gain or Loss}\} \{\text{Spectral Filter}\} \{\text{Temporal Filter}\}$$

$$= \{N_e''(x, y, v, t) + N_b''(x, y, v, t)\} \{L_x L_y\} \left\{ \frac{\pi r_l^2}{4\pi z_l^2} \right\} \{GF(v) T(t)\}$$

where $N_b''(x, y, v)$ is any background emission per unit area, including scattered laser light, dark current, and ambient light; L_x and L_y are the dimensions of the measuring volume per pixel related to the pixel size, l_x, and magnification, m, by $L_x = l_x/m$; r_l is the radius of the limiting aperture in the collection optics; z_l is the distance from the laser sheet to the limiting aperture; G allows for the losses from lens and filter surfaces ($\sim 4\%$ for normal incidence on an uncoated surface) and the photon gain from intensification (if used); $F(v)$ is the spectral transmittance function of any filters used and/or the wavelength shift produced by the intensifier; $T(t)$ is the transmission function of the shutter or gating electronics which can be integrated out if it is longer than the longest species emission lifetime.

The fraction of the light emitted by the tracer species which is actually observed in the camera is controlled by the limiting aperture (often the first lens) in the collection optics. The signal level per pixel is related to the lens $f \#$ (ratio of focal length to lens diameter) and the magnification, m, by the following relation:

$$N_{pp}(x, y, v, t) \propto L_x L_y \frac{r_l^2}{4 z_l^2} \propto \frac{l_x l_y}{16(1+m)^2} \frac{1}{(f \#)^2} \tag{7}$$

For a fixed laser energy and collection optics $f \#$, the signal levels will vary inversely with the sheet height. If the laser sheet fills the field of view, the signal levels scale as $m/(1+m)^2$.

For a fixed field of view, the signal levels scale inversely as the square of the $f \#$ and the signal to noise ratio will scale as the inverse of $f \#$ in the shot noise limit. Low $f \#$ number lenses are thus very desirable. The effective focal length of a given lens can be reduced by extension tubes or with the appropriate close-up lens. However, low $f \#$ lenses provide a very small depth of field and require accurate focussing as discussed below.

Commerical camera lenses are designed for infinite conjugate ratios ($m \rightarrow 0$) and to match the spatial resolution of film (~ 6 µm grain size). In PLIF experiments the magnification is often much larger and arrays with large pixels are desirable for improved signal levels. Using these lenses with large-pixel arrays results in aliasing of all frequencies above the Nyquist frequency of the array, i.e. the information in the high spatial frequencies folds over into the lower frequencies causing spurious signals (Pratt 1978). Low $f \#$'s reduce aliasing problems by degrading lens performance, but the contrast transfer function at the Nyquist frequency is also reduced (van Cruyningen, 1990).

The target shown in Fig. 3 was developed to aid in focussing and to allow direct measurement of the magnification, contrast transfer function, and image registration under experimental conditions. It is produced from a PostScript™ program and can be readily printed at low cost by commercial printers at 2,400 lines per inch on a Linotronic™ printer. The aspect ratio, the overall size, and the line thicknesses can be adjusted to match the array size, field of view, and pixel
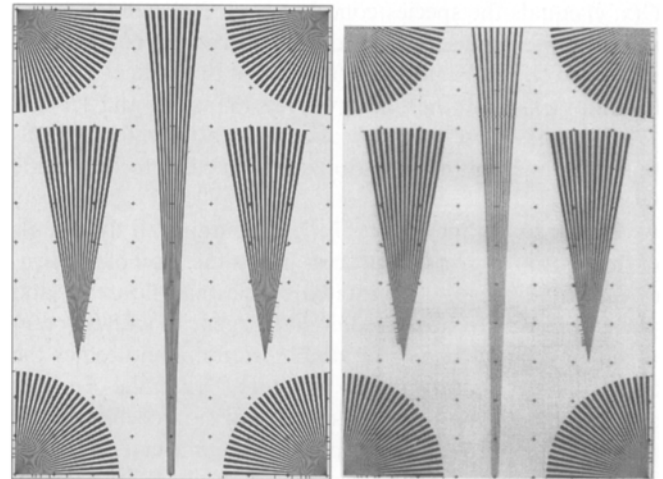

Fig. 3. Focussing target and camera image of target

dimensions in the experiment, respectively. This target is aligned with the laser sheet in the flow facility and the three center fans are used for the coarse focussing. As the target comes into focus, contrast reversals, as well as Moire Patterns, will appear in the four corner fans. The contrast reversal is illustrated in Goodman (1968) and is analyzed in Born and Wolf (1980). The width of each black or white line in the corner fans is four pixels at the maximum radius. The lens and array cutoff frequencies are matched when the first contrast reversal occurs at one quarter of the corner fan radii, i.e. the point where the rays are one pixel width wide. When the contrast reversal occurs at the same radius in all four fans, the array will be square with the target. The center fan is curved so the spatial frequency varies from 0.25, 0.5, 1.0, and 2.0 line pairs per pixel at the top, one-third, two-thirds, and bottom of the target, respectively. This fan allows detailed measurement of the contrast transfer function under actual experimental conditions.

The collection optics must be checked for two additional possible errors, namely geometric distortion and flat field non-uniformities. Short focal length lenses produce barrel distortion. The regularly spaced crosses in the target of Fig. 3 provide registration points to allow calculation of warping coefficients during image correction. Further, at low $f \#$'s, points far from the optical axis do not present the limiting aperture with the same solid angle as points close to the axis. Thus a uniformly lit target will appear dimmer near the edges of the image. This effect can be corrected by dividing the flowfield images by an image of a flat field. The flat field can be produced by either 1) an array of a large number of light emitting diodes behind a frosted glass plate, 2) an integrating sphere, or 3) a uniformly lit fluorescent surface.

6 Camera characterization

The camera converts the incident photons to electrical charge, which in turn produces an output voltage. This

voltage is amplified, digitized, and stored on a computer. Following Janesick et al. (1985) or Janesick et al. (1987), the digital signal level observed per pixel is

$N_D(x, y) = \{$Incident Photons$\} \{$Electrons per Photon$\}$

$\cdot \{$Volts per Electron$\} \{$Amplification$\}$

$\cdot \{$Digital Units per Volt$\}$

$$= \int_v N_{pp}(x, y, v)\, \eta_E(v)\, S_v\, A_1\, A_2\, dv \qquad (8)$$

where N_{pp} is the number of incident photons as derived in the previous section integrated over the exposure time; η_E is the quantum efficiency of the array in electrons per photon; S_v is the array sensitivity in volts per electron; A_1 is the analog amplification of the signal; A_2 is the analog to digital conversion setting in digital numbers (DN) per volt.

The last three constants are normally grouped as $K = (S_v A_1 A_2)^{-1}$ [e$^-$/DN], since they depend only on the camera settings and can be measured once for an experiment. They can be experimentally determined by the photon-transfer technique for shot-noise limited operation. For the Photometrics camera at operating conditions $K \sim 1.3$ [e$^-$/DN] and $\sigma_R \sim 18$ DN $= 24$ e$^-$. The dark current was measured to be less than ten counts per minute at 153 K, so for the millisecond exposure times used, the dark current is negligible relative to the analog amplifier noise.

The variation of quantum efficiency with wavelength can be measured with a greybody source (tungsten lamp) and a prism spectrograph (van Cruyningen, 1990). Thompson specifies a quantum efficiency of $\sim 30\%$ for the array at the peak of the biacetyl phosphorescence (520 nm). The pixel-to-pixel uniformity for flat field illumination was measured to be better than 1%. The linearity of the array sensitivity, S_v, was observed to be better than one-half of one percent in a series of images with different exposure times. The linearity of the analog amplifier gain, A_1, was checked in a series of exposures of a constant light source, taken at different gains. The deviation from linearity was less than 0.5%. Finally the reciprocity, i.e. a short exposure at high gain vs. a long exposure at low gain, was verified to be within 1.0%.

7 Experimental resolution

The derivations of the previous sections will now be applied to find values for the six parameters describing a PLIF experiment, namely the spatial resolution, the spatial dynamic range, the minimum detectable signal, the signal dynamic range, the temporal resolution, and the framing rate.

The measuring volume size is determined by the magnification of the collection optics, the pixel size, and the sheet thickness. For a field of view of 45 nozzle diameters (45 cm) the magnification was 1/34. The camera pixel size (23 × 23 μm) gives a measuring volume of $0.8 \times 0.8 \times 0.6$ mm per pixel. The last dimension comes from the sheet thickness as measured by traversing a knife edge across the beam and measuring its attenuation with a photodiode.

In accordance with the Nyquist theorem, the smallest observable spatial scale is twice the measuring volume size. The largest observable spatial scale is of the order of the field of view. For a 576×384 pixel array the spatial dynamic range is thus 288×192.

The minimum detectable signal occurs for a signal to noise ratio of 1.0. This corresponds to the noise floor, $\sigma_R = 18$ DN $= 24$ e$^-$. Using $\eta_E = 0.3$ at 520 nm (the peak of the biacetyl emission) in Eq. (8), gives $N_{PP} \geq 80$ photons per pixel. To find the equivalent biacetyl concentration, the equations from the earlier sections are invoked. The collection optics consisted of one $f \# 1.2$ lens with a two diopter close-up lens to give an effective $f \#$ of 1.09. No filter was required to block scattered light from the laser since the quantum efficiency of the array is effectively zero at 351 nm ($F(v) = 1$ in Eq. (6)). The 50 ms shutter time was much longer than the biacetyl phosphorescence lifetime, so all the emission is collected and $T(t) = 1$. The lens consisted of a number of elements in several groups, but the internal surfaces are coated. The loss is thus taken to be $G \sim 0.92$. Using a magnification of 1/34 in Eq. (6) gives 2.4×10^{-7} photons collected per pixel per (photon/cm^2) emitted. About one out of every four million photons emitted per cm^2 by the biacetyl is imaged onto a single pixel for this large magnification. For $N_{PP} \geq 80$ photons per pixel requires $N_e'' \geq 3.3 \times 10^8$ photons/cm^2, neglecting the background emission.

The emission versus laser power data gives 1.3×10^{-5} photons/cm^2 emitted per incident photon/cm^2. For 32 torr partial pressure biacetyl, Eq. (2) gives $\alpha \eta_s \cong 1.1 \times 10^{-23}$ cm^2 *. This value may now be used to estimate the corresponding biacetyl concentration in the imaging experiments. A laser intensity of 100 mJ at 351 nm (8.55×10^{14} Hz) over a 45 cm high sheet gives 4.0×10^{15} photons incident per cm height. Using $N_e'' \geq 3.3 \times 10^8$ in Eq. 4.1, the minimum detectable biacetyl concentration is 7.5×10^{15} cm^{-3} or 280 ppm.

The signal dynamic range is limited by the lesser of the range in detectable biacetyl concentrations, the pixel well depth, or the analog to digital convertor range. The saturation biacetyl concentration is 50,000 ppm, so a minimum detectable signal of 280 ppm gives a dynamic range of 180. The pixel well depth is 350,000 e$^-$ and the camera noise floor is 24 e$^-$ which gives a dynamic range of 14,600. Finally the A/D convertor digitizes to 14 bits which gives a dynamic range of 16,000. The signal dynamic range is limited by the large field of view in these experiments. For fixed laser energy and fixed collection optics $f \#$, the signal dynamic range varies inversely with the height of the laser sheet.

The 50 ms shutter time in this experiment was significantly longer than the phosphorescence lifetime, so the latter limits the temporal resolution. The phosphorescence decays to its 1/e value in 1.1 ms (van Cruyningen, 1990). If one

---

* For excitation at 420 nm, $\alpha \cong 8 \times 10^{-20}$ cm^2 (Okabe and Noyes, 1957) and $\eta_s \cong 0.15$ (Epstein, 1974). These values provide much higher conversion efficiencies compared to pumping at 351 nm, but a 420 nm excitation source was not available at the time of the experiment

adopts a stringent blurring criteria that not more than two pixels should detect emission from the same fluid element, i.e. a fluid element does not move more than one measuring volume distance during the exposure time, then the phosphorescence lifetime limits the flow velocities to less than ~ 2 m/s at this magnification. This is valid for downstream distances greater than 20 jet diameters.

The framing rate in this experiment was 0.03 Hz since double-correlated sampling was required to reduce the noise in the charge to voltage conversion during the array readout.

8 Image corrections

The analysis of the experimental components given in sections 3–6 provides the framework for correction of the experimental images. The errors accumulate as the signal propagates through the experiment, so they are best corrected in the reverse order. The functional dependence of all the corrections is given below. Functions of x and y are images which result in image operations; functions of either x or y are vectors which result in row or column operations on an image; functions of digital number (DN) are functional remappings of the image data; and constants result in scaling of the entire image.

– First the flowfield image is divided by an image of the non-uniformities in pixel response, $U(x, y)$. This is an image of a flat field taken without any lenses in front of the array. If the camera response is not a linear function of incident light, this correction will be a function of DN as well: $U(x, y, \text{DN})$. This will necessitate a (possibly different) remapping at each pixel. Point defects in the array, i.e. 'dead pixels' are replaced with the average value of their neighbors.

– The previous result is warped using the image registration function, $R(x, y; x', y')$, to correct for any geometric distortion in the collection optics. This function is a bilinear interpolation whose coefficients are determined from the registration points in an image of the focussing target.

– The geometrically corrected image is divided by the flat field non-uniformity of the collection optics, $FF(x, y)$. To determine $FF(x, y)$, an image of a uniform light source is taken with the identical optics as used in the flowfield image acquisition. The corrections described above are then applied to the flat field image to produce $FF(x, y)$. For low $f \#$ lens configurations points located off the axis in the object plane view a smaller solid angle of the lens. This deviation follows the Lambertian cosine law.

– Following the flat-field correction, the background light $N_b''(x, y)$, is subtracted. This image is acquired with no tracer in the flow, but the laser still firing and is corrected with the steps described above. This correction includes subtraction of the dark current and subtraction of any scattered laser light.

– The Stern-Vollmer factor may not be a linear function of concentration if self-quenching occurs, or it may not be a linear function of laser energy near saturation intensities.

In these situations each pixel must be remapped using the inverse of the actual functional dependencies, $N(N)$ and $I(I)$.

– If the optical depth of the seeded flow is of the same order as the flow width, corrections for beam attenuation must be applied. From Eq. 4.1, the x dependence is

$$N_e''(x) \propto e^{-(\alpha+\sigma)\int C(x)\,dx}\,C(x) \tag{9}$$

The multiplicative correction factor, $OD(x)$, is given by solving the following equation pixel by pixel in a predictor-corrector scheme following the path of the laser beam:

$$OD(x) = (e^{-(\alpha+\sigma)\int C(x)\,dx})^{-1} \tag{10}$$

The initial estimate for $C(x)$ is the pixel value where the beam enters the image. An estimate of the correction, and thus $C(x)$, is calculated stepping forward pixel by pixel. The estimate is derived by taking a derivative of digital data and thus is very susceptible to noise. Averaging over several rows or fitting earlier points with a cubic spline improves the result.

– The laser sheet is normally not uniformly distributed with height. This results in a laser sheet correction where each row in the flowfield image is divided by $\phi_i'(y)$. If the laser sheet is not collimated, a sheet image is required for this correction. The sheet image must be processed using the aforementioned procedures.

– Finally, the images have to be normalized by the number of photons in the laser pulse, N_i. This is simply a multiplication of the entire image by a constant.
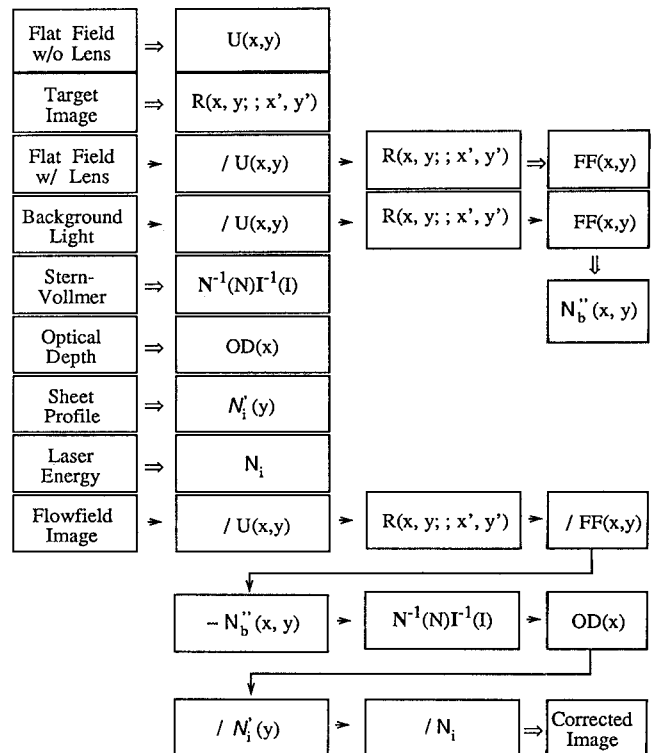

Fig. 4. Image correction procedure

These correction steps are illustrated in Fig. 4. This is an extensive list of possible error sources and not all corrections will be applicable in every experiment. If, for example, the geometric distortion in the collection optics is negligible, the two flat field corrections can be combined. In the applications of these corrections numerous division steps occur. If the divisor is a small number at any pixel in the image, the operation will produce very large values at that pixel. These operations will tend to accentuate the noise in the darker areas of the original image. This effect can be overcome by using Weiner filtering techniques as described in Pratt (1978).

9 Results

Figure 5a shows an image of the first 45 diameters of an isothermal turbulent jet ($Re = 8,500$). To the left of the image are three cross-sections at the locations shown by lines in the image and to the right of the image is a streamwise section. Figure 5b is a fully corrected image. The instantaneous concentrations were measured to 1.5% accuracy for points within an image and approx. 2% between images.

Figure 6a shows the mean concentration obtained by averaging 25 instantaneous frames. The centerline values in the mean image were fit to the self-similarity law (Tennekes and Lumley 1978),

$$C(x, 0) = C_0 \frac{K}{} \tag{11}$$

where x_0 is a virtual origin for the jet; C_0 is the centerline concentration at the virtual origin; and K is the decay constant.

Rescaling of the images according to self-similarity (Fig. 6b) allows pixel values at all downstream locations to be directly compared. The cross stream profiles of the mean jet tend towards a Gaussian profile, whereas the instantaneous profiles have very steep edges.

The root-mean-square concentration fluctuations shown in Figure 7a were calculated by subtracting the individual images from the mean image, squaring and summing the difference images, and dividing by the total number of images. Large-scale motions of the jet produce most of the fluctuations near the jet exit, but variations internal to the jet dominate further downstream. On average, the rms concentration fluctuations at a pixel were 34% of the mean value at that pixel.

Figure 7b is an instantaneous image of

$$E = \left(\frac{\partial C}{\partial x}\right)^2 + 2\left(\frac{\partial C}{\partial y}\right)^2 \tag{12}$$

which is an approximation to the scalar dissipation in this jet. The measuring volume dimensions are approx. eight times the Kolmogorov scale size at forty diameters downstream, so the gradients are taken over several Kolmogorov scales. Dowling (1988) has shown this may be sufficient to resolve all the spatial scales in the flow. The factor of two in (12) is due to the assumption that the radial and axial gradients are equal (Namazian et al. 1988). Figure 7c is an aver-
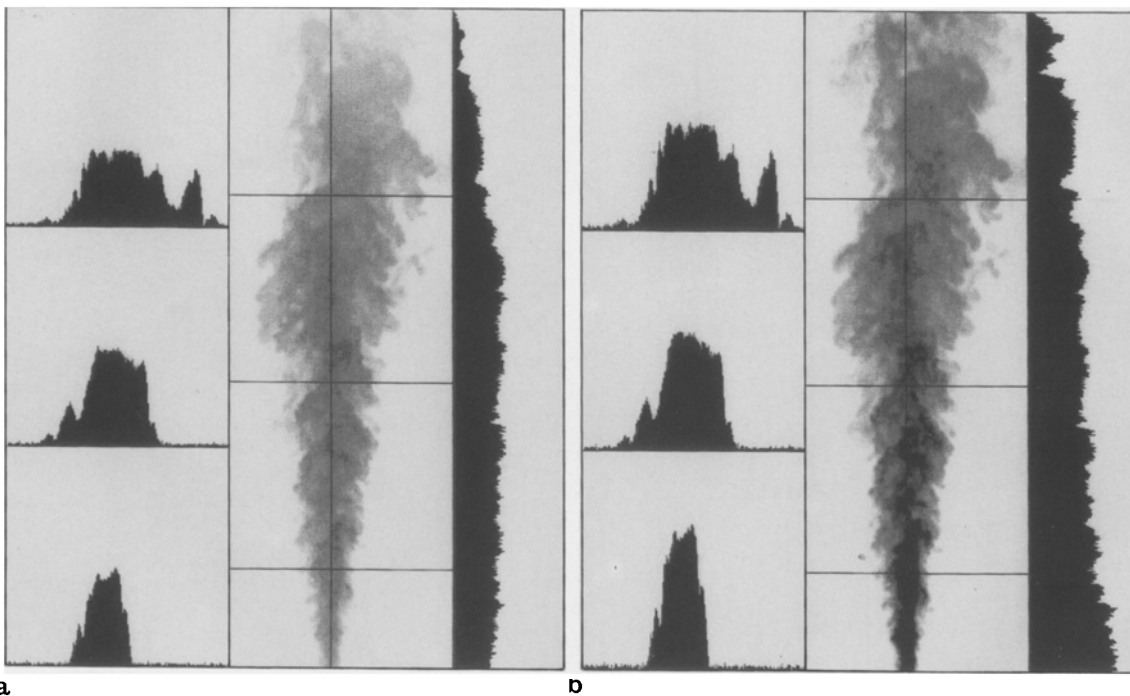

a   b

Fig. 5a and b. Instantaneous concentration in a turbulent jet; **a** image of biacetyl concentration in first 45 diameters of a $Re = 8,500$ nitrogen jet seeded with 5% mole fraction biacetyl; **b** image corrected for lens response, background light, laser sheet variations, and laser energy
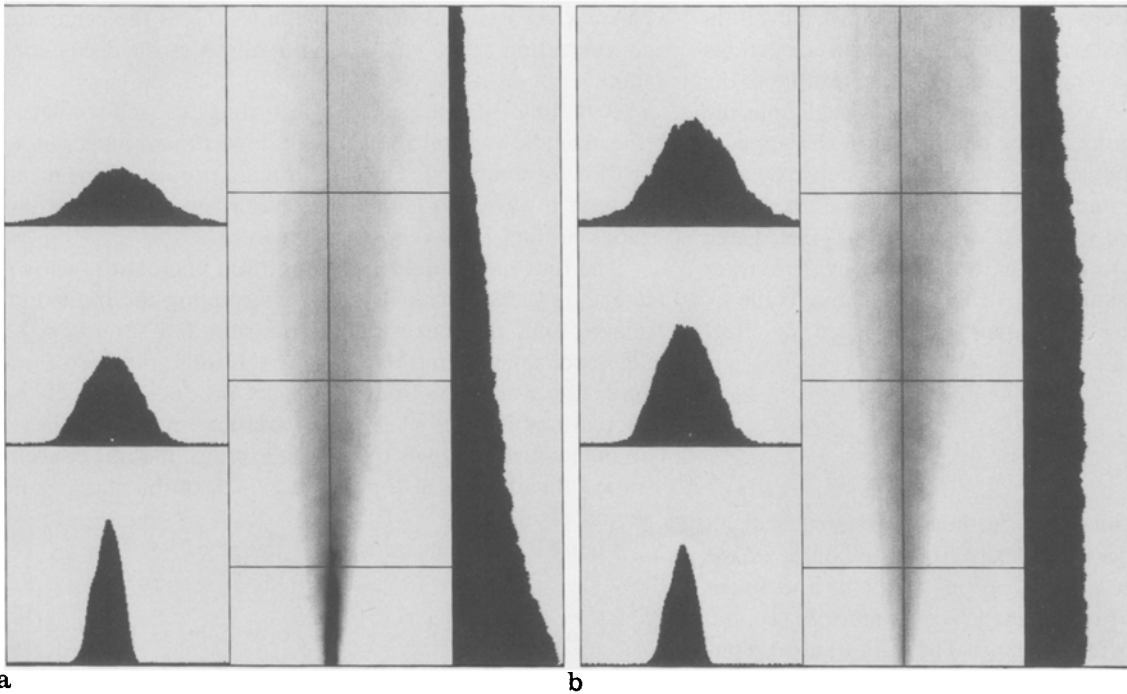
Fig. 6a and b. Mean concentration in a turbulent jet; **a** concentration averaged over 25 frames; **b** mean concentration image scaled according to self-similarity constants determined from a centerline fit of the data
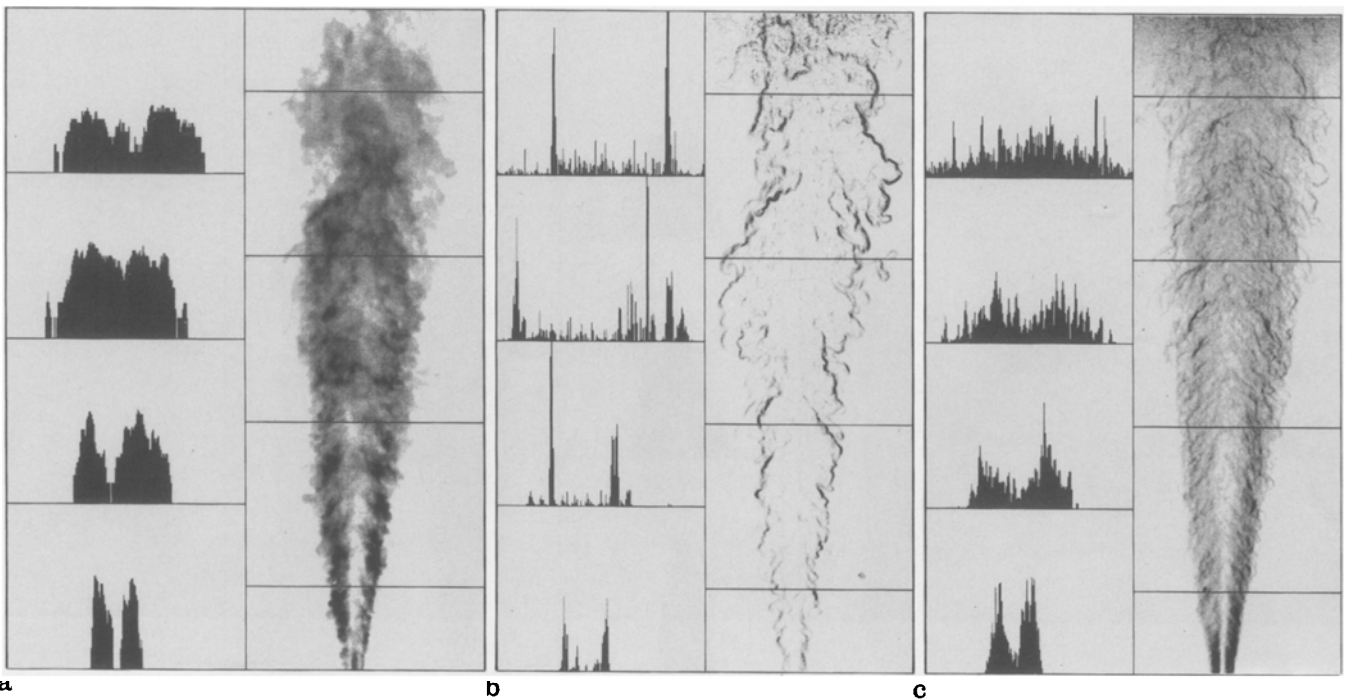

Fig. 7a–c. RMS concentration fluctuations and dissipation in a turbulent jet; **a** RMS fluctuations calculated over 25 frames; **b** estimate of instantaneous dissipation; **c** average of 25 dissipation images

age of 25 instantaneous dissipation images. Note the lines of maximum dissipation are aligned with the principal axis of strain in this flow.

10 Conclusions

A framework for analyzing the propagation of signals through a PLIF experiment has been developed. The error sources have been quantified and the image corrections detailed. An experiment involving concentration measurements of the molecular tracer biacetyl in a turbulent jet has illustrated the application of the experimental method. Images of the instantaneous, average, root-mean-square, and dissipation of concentration illustrate the investigative power and resolution of the PLIF technique. This flow visualization technique can provide accurate, quantitative data at all points in a plane simultaneously which is of great value in studies of mixing and turbulent structure.

Acknowledgements

References

Allen, M. G. 1987: Digital imaging techniques for single and multiphase reacting flows. PhD Thesis in Mechanical Engineering, Stanford University

Born M.; Wolf, E. 1980: Principles of optics. New York: Pergamon

Cattolica, R. J.; Vosen, S. R. 1985: Two dimensional measurements of OH in a constant volume combustion chamber. 20th sym. (int.) on combustion, Pittsburgh 1985

Dahm, W. J. A.; Dimotakis, P. E. 1987: Measurements of entrainment and mixing in turbulent jets. AIAA J 24, 1216–1233

Dimotakis, P. E.; Miake-Lye, R. C.; Papantoniou, D. A. 1983: Structure and dynamics of round turbulent jets. Phys Fluids 26, 11, 3185–3192

Dowling, D. 1988: Mixing in gas phase turbulent jets. PhD Thesis in Mechanical Engineering, California Inst. of Technology

Dyer, M. J.; Crosley, D. R. 1982: Two-dimensional imaging of OH laser-induced fluorescence in a flame. Opt Lett 7, 8, 382–384

Epstein, A. H. 1974: Fluorescent gaseous tracers for three dimensional flow visualization. GTL, Mass. Inst. of Technology, Report no. 117

Goodman, J. W. 1968: Introduction to fourier optics. New York: McGraw-Hill

Hanson, R. K. 1987: Combustion diagnostics: Planar imaging techniques. In: Twenty-first symposium (International) on combustion. The Combustion Institute 1677–1691

Hiller, B. 1986: Combined planar measurements of velocity and pressure fields in compressible gas flows using laser-induced iodine fluorescence. PhD Thesis in Mechanical Engineering, Stanford University

Janesick, J.; Klaasen, K.; Elliot, T. 1985: CCD charge collection efficiency and the photon transfer technique. In: Solid State Imaging Arrays. (eds. Prettyjohns, K. N.; Dereniak, E. L.) Proc. SPIE 570, 7–19

Janesick, J. R.; Elliot, T.; Collins, S.; Blouke, M. M.; Freeman, J. 1987: Scientific charge coupled devices. Opt Eng 26, 8, 622–714

Kychakoff, G.; Howe, R. D.; Hanson, R. K.; McDaniel, J. C. 1982: Quantitative visualization of combustion species in a plane. Appl Opt 21, 18, 3225–3227

Kychakoff, G.; Howe, R. D.; Hanson, R. K. 1984: Quantitative flow visualization technique for measurements in combustion gases. Appl Opt 23, 5, 704–712

Kychakoff, G.; Paul, P. H.; van Cryningen, I. L.; Hanson, R. K. 1987: Movies and 3-d images of flow fields using planar laser-induced fluorescence. Appl Opt 26, 2498–2500

Liu, H.-T.; Lin, J.-T.; Delisi, D. P.; Robben, F. A. 1977: Feasibility study of a dye-fluorescence technique for measuring concentrations in fluids. NBS Special Publication no. 484, Proc. of the symposium on flow in open channels and closed conduits held at NBS, Gaithersburg, MD, Feb 23–25

Liu, J. B.; Pan, Q.; Liu, C. S.; Shi, J. R. 1988: Principles of flow diagnostics by laser induced biacetyl phosphorescence. Exp Fluids 6, 505–513

Namazian, N.; Scheffer, R. W.; Kelly, J. 1988: Scalar dissipation measurements in the developing region of a jet. Comb and Flame 74, 2, 147–160

Okabe, H.; Noyes, W. A. 1957: The relative intensities of fluorescence and phosphorescence in biacetyl vapor. J Am Chem Soc 79, 801–806

Paul, P. H.; van Cruyningen, I.; Hanson, R. K.; Kychakoff, G. 1990: High resolution digital flow-field imaging of jets. Exp Fluids (in press)

Piepmeier, E. H. 1972: Theory of laser saturated atomic resonance. Spectrochimica Acta 27B, 431

Pratt, W. K. 1978: Digital image processing. New York: Wiley Interscience

Shlien, D. J. 1988: Instantaneous concentration field measurement technique from flow visualization photographs. Exp Fluids 6, 541–546

Tennekes, H.; Lumley, J. L. 1972: A first course in turbulence. Cambridge, MA: MIT Press

van Cruyningen, I. J. 1990: Quantitative planar laser-induced fluorescence imaging in turbulent gaseous jets. PhD Thesis in Mechanical Engineering, Stanford University

Vincenti, W. G.; Kruger, C. K. 1982: Physical gas dynamics. Malabar, Florida: R. E. Kreiger

Winter, M.; Lam, J. K.; Long, M. B. 1987: Techniques for high-speed digital imaging of gas concentrations in turbulent flows. Exp Fluids 5, 177–183